# Supporting Information

Volfson *et al.* 10.1073/pnas.0706805105

## SI Text

### Methods

**Microfluidics.** The overall design of our microfluidic device was based on the Tesla microfluidic chamber design developed in ref. 1 for use with *Saccharomyces cerevisiae*. The original Tesla microchemostat (T$\mu$C) design implemented the classic Tesla diode loop (2–4) modified for imaging a monolayer culture of growing yeast cells. We made several modifications to adapt it for application to *E. coli* (Fig. S1*A*). First, we lowered the height of the diode side-arm, which forms the shallow trapping region capable of constraining a population of cells to a common focal plane. For imaging yeast cells, the cell-trapping region was fabricated to be 4 $\mu$m high, which is the approximate diameter of a yeast cell. For imaging *E. coli* cells, we lowered this height to 1 $\mu$m, which is the approximate diameter of a cylindrical *E. coli* cell of the K-12 MG1655 strain. To maintain the proper resistance ratio for flow splitting, we also lowered the delivery channel height to 3 $\mu$m. Last, the cell-trapping region was split into three parallel channels for simultaneous observation of three isolated *E. coli* colonies. The width of each parallel chamber was limited to 30 $\mu$m so as not to exceed the width/height aspect ratio of 30 for PDMS and risk structural collapse of the chamber "ceilings."

To achieve long experimental runs, a critical design objective was to avoid clogging between the media inlet and the trapping region. We developed a three-port chip design in which the main channel extending from the cell port splits into a media channel and a waste channel downstream of the trapping region. Once cells are loaded, they receive nutrients via a combination of diffusion and advection. Supplied with abundant nutrients, the cells are able to grow exponentially to fill the trapping region in a monolayer. The open walls of the trapping region allow for peripheral cells to escape when they are pushed into the high flow of the main channel, thus permitting continuous exponential growth long after the trapping region fills.

**Microscopy and Image Analysis.** All images were acquired by using a Hamamatsu Orca-ER cooled-CCD camera mounted on a Nikon Diaphot TMD inverted microscope. A graphical user interface written in LabVIEW (National Instruments) controlled the automated acquisition of bright-field images and provided scanning capability via motorized axis control. At each time point, three slightly overlapping images were collected at $\times$100 magnification. The high magnification provided a large number of pixels per cell to aid in image segmentation, while scanning allowed the imaging of many cells. Proper focus was maintained throughout each experiment via manual adjustment.

After each imaging session, a complete profile of the system at each time point was assembled by stitching together the three overlapping images. For each of these merged images, the positions and orientations of individual cells were determined by using a custom image segmentation software suite written in IDL (ITT Visual Information Solutions). Each composite image was processed by using standard grayscale morphology techniques as reported (1). The major steps of the recognition process are shown in (Fig. S1 *B–D*). To determine the coarse-grained velocity profiles averaged across the channel, we used the standard particle-image velocimetry technique based on the Minimum Quadratic Difference method (5), followed by filtering using the local signal-to-noise ratio (6).

**Overview of the Experiments.** In our experimental studies of bacterial colony growth, we used strains of *E. coli* that lack flagella. These cells had a rod-like shape with a length-to-diameter ratio that varied between 2 and 5, depending on the age of the cell (Fig. S1*B*). For experimentation, the cells were loaded into the three channels of the microfluidic device by directing flow in the "forward" direction. Upon trapping a few cells in each region, the flow was reversed and slowed to steadily supply fresh nutrients to the cells over an experimental duration of $\approx$4–6 h. Cells continued to grow and fill the chambers during this time, while images were periodically acquired in the bright-field channel at 2-min intervals. Extended runtimes were possible because of the use of fluid flow to continuously purge peripheral *E. coli* cells growing beyond the channel boundaries. For optimal *E. coli* growth, chip temperature was maintained at 37°C by flowing heated water through deep thermal channels fabricated into the device.

Additionally, we performed two experiments to measure the time scales of nutrient distribution over the field of view in our channel. In the first experiment, we introduced a red fluorescent dye with a molecular weight similar to that of the largest cell nutrient to the flow of media at a precise time and measured its diffusion into an empty cell-trapping region. We recorded the fluorescence averaged both within one region in the 3-$\mu$m-thick bypass channel and within three distinct regions in the cell-trapping area distributed over the field of view of the original experiment (left cyan, middle orange, and right red boxed regions in Fig. S2). We observed uniform distribution of the dye throughout the field of view within 2–3 min after introduction (Fig. S2 *A* and *C*). We also observed a slow upward trend in concentration after the fast initial transient, which was evidently caused by variation in dye concentration within the thick bypass channel. Indeed, after rescaling the fluorescence signal in the bypass channel by a factor of 1:2.5, it matched the fluorescence signal within the cell trapping region very well. We attribute the observed deviation in the scaling coefficient from the nominal ratio of depths for shallow and deep channels (1:3) to the nonlinear relationship between the depth of a layer and its integral optical fluorescence.

To examine any difference in diffusion time scales in a full channel, we next repeated this experiment in a chamber packed with cells. Although our intention was to conduct this experiment at the fully packed limit, some empty pockets of media remained in the cell-trapping channels caused by bulk cell flow (Fig. S2 *B* and *D*). In this experiment, fluorescence measured within the regions filled with cells was $\approx$60% smaller than within the empty regions of the channel. This was to be expected, because a large volume fraction of the channels is filled with nonfluorescing cells. Despite the presence of the cells, the dye distribution again quickly became nearly uniform within the field of view (after $\approx$5–10 min; Fig. S2 *B* and *D*), indicating fast nutrient delivery to the cells. Additionally, we took advantage of the empty regions in this experiment to compare the fluorescence in an empty channel region with the fluorescence in the thick bypass channel region (rescaled by using the same 1:2.5 ratio as in the empty channel experiment). As Fig. S2*D* shows, these two curves approach each other after $\approx$15 min. The time to reach equilibrium is longer in this case because the selected empty area is significantly further away from the inlet than our typical experimental region.

In summary, we have confirmed through experimentation that the volume concentration of nutrients in the working area

becomes uniform on a time scale of 5–15 min for both empty and full channels, which is much faster than the time scale of colony development. Thus, the growth rates of our experimental colonies should not be limited by poor nutrient delivery.

### Continuum Description of the Bacterial Growth and Ordering

**General Description.** The continuum description of cell ordering is similar in spirit to the phenomenological Landau-de Gennes theory developed for dense liquid crystals and polymeric solutions (see, e.g., ref. 7). Each cell is characterized by a unit pseudovector $\mathbf{u}$ specifying the orientation of the cell ($\pm\,\mathbf{u}$ directions are equivalent because cells are assumed apolar). While the mean $\langle\mathbf{u}\rangle$ is zero because of the reflection symmetry of cells, the distribution of cell directions $\Psi(\mathbf{u})$ can become anisotropic. The anisotropy of the distribution is characterized by the tensor order parameter $\mathbf{Q}$ with components

$$Q_{ij} = \langle u_i u_j - d^{-1}\delta_{ij}\rangle, \qquad \textbf{[S1]}$$

where $i, j \in x, z$, $\delta_{ij}$ is the Kroneker symbol, $d$ is the number of space dimensions, and brackets denote averaging over the mesoscopic volume. Tensor $\mathbf{Q}$ is symmetric and traceless, and in two dimensions it can be written in the form:

$$Q_{ij} = 2Q\left(n_i n_j - \frac{1}{2}\delta_{ij}\right), \qquad \textbf{[S2]}$$

where $n_i$ are components of the Frank director (the unit vector aligned with the mean orientation of the cells in a mesoscopic volume), and $Q \equiv \sqrt{{Q_{xx}}^2 + {Q_{xz}}^2}$ is the scalar order parameter (the eigenvalue of $\mathbf{Q}$).

In the theory of liquid crystals, the continuous description of nematics is typically based on the equations for the director field and the velocity field (8). Such a description works well below the critical point and when the scalar order parameter is everywhere close to unity. However, close to the isotropic-nematic transition, the magnitude of the order parameter changes significantly, and more general equations of nematohydrodynamics incorporating the orientational order parameter are used (9). Here, we adopt this description with some important modifications resulting from the differences between rod-like molecules and macroscopic rod-like cells. One such difference is that cells are much less influenced by thermal fluctuations, and accordingly, free-energy minimization plays a minor role in the dynamics of the order parameter. Second, unlike molecules, living cells grow and divide, and this process profoundly alters the collective dynamics.

Let us first present the standard set of equations of "nematohydrodynamics" (9) and then introduce the differences caused by the cell dynamics. Flows of liquid crystals usually are sufficiently slow to neglect compressibility and assume constant volume density, which leaves only two equations: one for the velocity field and another for the order parameter. The velocity equation has the usual form of momentum balance:

$$\frac{D\rho\mathbf{v}}{Dt} = -\nabla\cdot\sigma + \mathbf{f}, \qquad \textbf{[S3]}$$

where $D/Dt = \partial_t + \mathbf{v}\nabla$ is the material derivative, $\rho$ is the density, $\sigma$ is the stress tensor, and $\mathbf{f}$ is the volume force. The local dynamics of the order parameter are described by the equation:

$$\frac{DQ_{\alpha\beta}}{Dt} = \kappa^{[a]}_{\alpha\gamma}Q_{\gamma\beta} - Q_{\gamma\beta}\kappa^{[a]}_{\alpha\gamma} + B\kappa^{[s]}_{\alpha\beta} + \Gamma H_{\alpha\beta}, \qquad \textbf{[S4]}$$

where $\kappa^{[a]}_{\alpha\beta} = (\partial_\alpha v_\beta - \partial_\beta v_\alpha)/2$ and $\kappa^{[s]}_{\alpha\beta} = (\partial_\alpha v_\beta + \partial_\beta v_\alpha)/2$ are the symmetric−traceless and antisymmetric parts of the strain rate tensor $\kappa_{\alpha\beta} = \partial_\alpha v_\beta$, respectively.

The last term in Eq. **S4** describes the entropic relaxation of the nonconserved order parameter caused by minimization of the free energy,

$$H_{\alpha\beta} = -\left[\frac{\delta F}{\delta\theta_{\alpha\beta}} - d^{-1}Tr\left(\frac{\delta F}{\delta\theta}\delta_{\alpha\beta}\right)\right]. \qquad \textbf{[S5]}$$

The free energy functional, $F$, has two parts,

$$F = F_{LG} + F_F, \qquad \textbf{[S6]}$$

where in 2D

$$F_{LG} = \int d\mathbf{x}\rho(\mathbf{x},t)[A_2 Tr(\mathbf{Q}\cdot\mathbf{Q}) + A_4(Tr(\mathbf{Q}\cdot\mathbf{Q}\cdot\mathbf{Q}\cdot\mathbf{Q})^2 + \ldots] \qquad \textbf{[S7]}$$

is the Landau-de Gennes free energy caused by the ordering of cells, and

$$F_F = \int d\mathbf{x}\rho(\mathbf{x},\,t)[K_1(\partial_\alpha Q_{\beta\gamma})^2 + K_2(\partial_\alpha Q_{\alpha\beta})^2] \qquad \textbf{[S8]}$$

is the Frank elastic free energy. Here, $A_2$ and $A_4$ are parameters dependent on the local cell density, $\rho(\mathbf{x}, t)$, and $K_{1,2}$ are elastic moduli.

Substituting **S2** into **S6**, we get

$$F = \int d\mathbf{x}\rho(\mathbf{x},\,t)[A_2Q^2 + A_4Q^4 + K_1(\partial_\alpha Q_{\beta\gamma})^2 + K_2(\partial_\alpha Q_{\alpha\beta})^2]. \qquad \textbf{[S9]}$$

To close this system of equations, a constitutive relation coupling the stress tensor to the strain and strain rate fields is needed. In the theory of liquid crystals (9), a linear constitutive relation is usually assumed,

$$\sigma_{\alpha\beta} = \beta_3\kappa^{[s]}_{\alpha\beta} - \beta_1 H^{[s]}_{\alpha\beta} + H^{[s]}_{\alpha\gamma}Q_{\gamma\beta} - Q_{\alpha\gamma}H^{[s]}_{\gamma\beta} - \frac{\delta F}{\delta\partial_\alpha Q_{\lambda\rho}}\partial_\beta Q_{\lambda\rho} - p\delta_{\alpha\beta}, \qquad \textbf{[S10]}$$

where the first four terms correspond to irreversible (viscous) stress and the last two terms describe reversible stress caused by distortion and isotropic pressure. $H_{\alpha\beta} = -\delta F/\delta Q_{\alpha\beta}$ is the molecular field. The pressure, $p$, is, of course, density-dependent, and it diverges as the density approaches the close-packing density limit. Note that in fact the close-packing density depends on the order parameter itself: for $Q = 0$, the rods are completely disordered, and the close-packing density is low (it depends on the aspect ratio of the rods, $l$, of course), whereas when $Q \to 1$, the close-packing density approaches 1. We will model this by choosing

$$p = P\exp[s(\rho - \rho_c)]. \qquad \textbf{[S11]}$$

This relation implies that the pressure is exponentially small for $\rho < \rho_c$ (parameter $s$ is large) and exponentially large for $\rho > \rho_c$. The close-packing density, $\rho_c$, is itself a function of the order parameter, $Q$, where more ordered populations have higher close-packing densities. We model this dependency by the relation, $\rho_c = \rho_c^d + (\rho_c^o - \rho_c^d)Q^2$.

To describe the "cellular fluid dynamics," we must take into account the fact that the density of cells can vary significantly both in space and time. Therefore, we must add a continuity equation for the cell density,

$$\frac{\partial \rho}{\partial t} + \nabla(\rho \mathbf{v}) = \alpha \rho. \quad \text{[S12]}$$

Here, the rhs describes the exponential growth of the cell mass.

If cells move in close proximity to the top and/or bottom plates, they experience drag caused by the wall friction. This effect can be described by including the volume force, **f**, which in the simplest approximation is linearly proportional to the cell velocity, **v**, such that $\mathbf{f} = -\mu\rho\mathbf{v}$. Thus, the momentum equation yields

$$\frac{D\rho\mathbf{v}}{Dt} = -\nabla\cdot\sigma - \mu\rho\mathbf{v}. \quad \text{[S13]}$$

In low-Reynolds number regimes typical for cell motion, the inertial effects can be neglected, and the momentum equation (**S3**) yields the velocity of cells as a gradient of the stress tensor,

$$\mathbf{v} = \mu^{-1}\nabla\cdot\sigma. \quad \text{[S14]}$$

However, as we shall see, using the full momentum equation (**S13**) yields a better agreement between the continuum theory and our numerical simulations.

The set of equations (**S4**–**S13**) form the basis for a study of cell growth and transport. However, to simplify the problem, in the following we take into account that the cells are only weakly affected by thermal fluctuations and therefore neglect thermodynamic effects. Specifically, we neglect the free-energy contributions to the order parameter dynamics and the stress tensor. Note that in this case Eq. **S4** does not guarantee that $Q < 1$ according to its definition. To uphold this condition heuristically, we multiply the rhs of Eq. **S4** by the scaling factor $1 - Q^2$. As a result, we arrive at the following set of equations:

$$\frac{DQ_{\alpha\beta}}{Dt} = (1 - Q^2)[\kappa^{[a]}_{\alpha\gamma}Q_{\gamma\beta} - Q_{\gamma\beta}\kappa^{[a]}_{\alpha\gamma} + B\kappa^{[s]}_{\alpha\beta}] \quad \text{[S15]}$$

$$\partial_t\rho + \nabla(\rho\mathbf{v}) = \alpha\rho \quad \text{[S16]}$$

$$\frac{D\rho\mathbf{v}}{Dt} = -\nabla p - \mu\rho\mathbf{v}. \quad \text{[S17]}$$

According to this set of equations, for a constant $\alpha$, the total mass of cells grows exponentially as $M \propto \exp(\alpha t)$. However, the outward flux of cells saturates the local growth of cell density at the expense of the exponential expansion of the area occupied by cells.

**Pressure-Independent Growth in One Dimension (Model A).** For the description of the expansion flow in a straight open channel, we can assume that all fields depend only on time and coordinate $-L < z < L$ along the channel. Therefore, this full set of equations can be reduced to a 1D model

$$\partial_t\rho + \partial_z(\rho v) = \alpha\rho \quad \text{[S18]}$$

$$\partial_t q + v\partial_z q = B(1 - q^2)\partial_z v \quad \text{[S19]}$$

$$\partial_t(\rho v) + v\partial_z(\rho v) = -\partial_z p - \mu\rho v, \quad \text{[S20]}$$

where $q \equiv Q \equiv Q_{zz}$, $v \equiv v_z$, $\alpha$ is the constant cell growth rate, $\mu$ is the bottom friction coefficient (we assume that the friction force is proportional to the cell velocity and independent of orientation), and the pressure, $p$, satisfies the constitutive relation (**S11**) discussed above.

The solution in which the density, $\rho(t)$, and the order parameter, $q(t)$, are independent of $z$; the velocity is a linear function of $z$ ($v = v_0(t)z$); and the pressure is parabolic ($p = p_0(t)(1 - z^2/L^2)$) satisfies Eqs. **S18**–**S20** at all times. The normalized "magnitudes" of this solution, $\rho$, $v_0$, $q$, and $p_0$, satisfy the set of three ODEs:

$$\dot{\rho} = \rho(\alpha - v_0) \quad \text{[S21]}$$

$$\dot{q} = B(1 - q^2)v_0 \quad \text{[S22]}$$

$$\dot{v}_0 = 2\rho^{-1}L^{-2}p_0 - (\alpha + \mu)v_0. \quad \text{[S23]}$$

Strictly speaking, the parabolic pressure profile and uniform density distribution do not satisfy the constitutive relation. However, because the dependence of pressure on the density is very sharp near the close-packing density of cells, the variations of density from the uniform state that account for a parabolic pressure distribution are very small and can be neglected. According to this set of equations, initially the density grows exponentially with rate $\alpha$ while the pressure remains low and the velocity gradient is absent. Once the density approaches the random close-packing density, $\rho_c$, the pressure begins to rise rapidly, and it produces a rapidly increasing expansion flow (Fig. 2). This flow removes excess cells from the channel and equilibrates the density at near the close-packed limit. There is a noticeable overshoot in the time dependence of the density that can be explained by the delay between the growth of the cells and the establishment of the flow (which has to overcome friction). This effect would be especially strong in long channels where the velocity at the ends of the channel has to reach large values. Initially, the density approaches the random close-packed density of cells. Subsequently, the expansion flow orients the cells along the channel axis, which in turn increases the close-packing density. Eventually, the system reaches a stationary regime with uniform density and velocity gradient, where cell growth is exactly balanced by the outgoing flux of cells. In this regime, $q_0 = 1$ and $\rho \approx \rho_c^o$. The velocity gradient, $v_0$, equals $\alpha$, and the corresponding pressure, $p_0$, equals $(\alpha + \mu)\rho_c^o\alpha L^2/2$. According to our model, cell density grows exponentially in the absence of flow and may only saturate when the velocity gradient reaches a value equal to the growth rate of the cells. For long channels, the establishment of the stationary velocity profile takes a long time, as the flow velocity has to overcome friction to reach high values near the open ends of the channels. This leads to the "overshoot" of the density, which then gradually diminishes as the velocity gradient increases.

Because the pressure scales as the square of the length of the channel, for long channels it reaches very high values in the middle of the colony. In fact, this high-pressure behavior is mitigated by the cell growth saturation. To simulate this effect, we used a modification of the growth model described in the next subsection.

**Pressure-Dependent Growth in One Dimension (Model B).** ODE model B has the same functional form (**S21**–**S23**); however, the growth rate $\alpha$ is assumed to be a function of pressure, $\alpha = \alpha_0[1 - (p/p_c)^2]$, such that cell growth terminates when the pressure reaches a critical value, $p_c$ (10). In fact, the pressure is not uniform across the channel; therefore the growth of cells will first saturate in the middle where the pressure is maximal, followed by propagation toward the channel periphery. However, in this simplified model we ignore this subtlety. It turns out that this approximation works quite well in describing the results of the DES (Fig. 2).

## Discrete Element Simulations

**Details of DES Algorithm.** To model the proliferation of cells in a microfluidic environment, we generalized an algorithm that we developed earlier to describe the dynamics of granular rods (11). This algorithm is based on the well known method of molecular dynamics (MD) simulations (12), which are used in different

areas of statistical physics. The main idea of the method is to follow the dynamics of the individual "particles" that constitute the system under study. In the case of a gas, these particles are molecules, and in the case of a granular material, each particle represents a single grain.

To simulate the motion, growth, and interaction of bacteria, we model every cell as a spherocylinder (circular cylinder with spherical caps) of diameter, $d$, total length, $l + d$, mass, $m$, and moment of inertia, $I$. In our 2D simulations, each rod has two translational and one rotational degree of freedom. The numerical algorithm that we used in our simulations is based on the "soft spheres" MD technique (13). The interaction between overlapping spherocylinders is modeled as the interaction between viscoelastic virtual spheres of diameter $d$ centered at the closest points between the axes of spherocylinders so that the cylinders are in contact whenever the virtual spheres are. The normal forces between virtual spheres are computed by using the Hertzian model, and the tangential frictional forces are computed by using dynamic Coulomb friction.

In our algorithm, two virtual spheres of diameter $d$, with centers at $\mathbf{r}_i$ and $\mathbf{r}_j$, and with velocities $\mathbf{v}_i$ and $\mathbf{v}_j$, interact via the force, $\mathbf{F}_{ij} = F_n\mathbf{n}_{ij} + \mathbf{F}_t$, where $F_n = k_n\delta^{3/2} - \gamma_n M_e \delta v_n$ is the normal force and $\mathbf{F}_t = -\gamma_t M_e \delta^{1/2}\mathbf{v}_t$ is the tangential force. The magnitude of the tangential force is bounded from above by the sliding friction force, $\mu_{cc}F_n$. Here, $M_e = M/2$ is reduced mass for cell–cell interaction, $M$ is the mass of a cell, $\delta = d - r_{ij}$ and $v_n = \mathbf{v}_{ij} \cdot \mathbf{n}_{ij}$ are the overlap and relative velocity in the direction of the normal, $\mathbf{n}_{ij} = (\mathbf{r}_i - \mathbf{r}_j)/r_{ij}$, and tangential direction $\mathbf{t}_{ij} = \mathbf{v}_t/v_t$ is specified by the relative tangential velocity, $\mathbf{v}_t = \mathbf{v}_{ij} - v_n\mathbf{n}_{ij}$. DES is performed in reduced units, and all quantities are normalized by an appropriate combination of the diameter, $d$, mass of virtual sphere, $m$, and gravitational acceleration, $g$. Typical values of material parameters are $k_n = 2 \times 10^6$ $(mg/d)$ and $\gamma_n = \gamma_t = 2.2 \times 10^2$ $(g/d)^{1/2}$. The coefficients of friction for cell–cell and cell–wall interactions are $\mu_{cc} = 0.1$ and $\mu_{cw} = 0.8$, respectively.

Once the forces arising from the interactions of virtual spheres are computed, they are applied to the cells. Cell motion is calculated by integrating Newton's equations for the forces and torques produced by interactions with the neighboring cells and walls of the chamber. Thus, the motion of every cell is described by the equations, $m\ddot{\mathbf{r}} = \mathbf{F}_e + \Sigma_c\mathbf{F}_c$ and $\mathbf{I}\cdot\dot{\boldsymbol{\omega}} = \Sigma_c(\mathbf{r}_c - \mathbf{r}) \times \mathbf{F}_c$, where $m$ and $\mathbf{I}$ are the mass and the tensor of inertia, respectively, $\mathbf{r}$ denotes the center of mass of the particle, $\boldsymbol{\omega}$ is the angular velocity, $\mathbf{F}_e$ represents external body forces, the sums run over the contact forces applied at every contact a given particle has (if any), and $\mathbf{r}_c$ defines the radius vector to the contact point. For modeling the body force caused by friction with the upper and lower walls of the channel, we used the Stokesian drag force, $\mathbf{F}_e = -\beta m\mathbf{v}$, with $\beta = 0.8$. With the forces and torques calculated, the equations of motion were integrated by using standard methods for ordinary differential equations.

When computing the stress tensor from DES, we used the following expression,

$$\sigma_{\alpha\beta}(\mathbf{x}) = \overline{\langle\sigma_{\alpha\beta}(\mathbf{x}, t)\rangle},$$

$$\langle\sigma_{\alpha\beta}(\mathbf{x}, t)\rangle = \left\langle \frac{1}{2}\sum_{c\neq i} r_\alpha^{ic}F_\beta^{ic} \right\rangle + \langle m^i\tilde{v}_\alpha^i\tilde{v}_\beta^i\rangle, \qquad \textbf{[S24]}$$

where

$$\alpha, \beta = \{x, z\}; \quad r_\alpha^{ic} = \mathbf{r}^{ic}\cdot\mathbf{e}_\alpha; \quad F_\beta^{ic} = \mathbf{F}^{ic}\cdot\mathbf{e}_\beta; \quad \tilde{v}_\alpha^i = v_\alpha^i - \overline{\langle v_\alpha^i\rangle};$$

$\mathbf{e}_\alpha$ denotes a component of the unit vector along the corresponding direction; $\mathbf{r}^{ic}$ is a radius vector from the center of mass of a cell to the point of contact; and indices $i$ and $c$ run over all cells and contacts, respectively. The overbar denotes a time average, and brackets denote an average within the mesoscopic volume much larger than the cell size and much smaller than the system size. The stress tensor in Eq. **S24** has two distinct components. The first one, virial or contact, describes pairwise interactions of grains. The second one, kinetic or Reynolds, is caused by velocity fluctuations.

Finally, we discuss the part of the algorithm that handles cell growth and division events. The length of a cell grows exponentially in time as $\exp(\alpha t)$ until it reaches a maximal length, $l_m$, which is drawn from a Gaussian distribution near a fixed length, $l_0$, with a coefficient of variation of 0.3. During the division event, the mother cell is replaced by two collinear daughter cells with lengths taken from a peaked distribution near $l_m/2$ to avoid spurious synchronization of cell division events. These daughter cells then continue to grow independently, with the repeated process of growth and division resulting in an exponential growth of the population.

**Results of Simulations, Models C1 and C2.** Cells were initially distributed uniformly in the cavity at low packing density ($\rho_0 = 0.02$) and random orientation. We imposed open boundary conditions at the ends of the channel so that cells reaching these ends were instantaneously removed from the system.

In model C1, the cell growth rate, $\alpha$, was fixed as in model A, and in model C2, the growth rate was scaled by the total pressure acting on each cell from its neighbors as in model B. Coarse-graining the positions, orientations, and velocities of individual cells, we analyzed the dynamics of the density, velocity, and order parameter fields. Representative profiles of longitudinal velocity, pressure, density, and order parameter are shown in Fig. 5 for different times from the beginning of the simulation and for different values of the aspect ratio, both for pressure-independent growth (model C1) and pressure-dependent growth (model C2).

We also used DES to fit the parameters of the continuum model (Fig. 2). Once the parameters were established, we compared DES with model predictions for the evolution of the density, velocity, order parameter, and pressure with constant and pressure-dependent growth starting from a low-density, disordered initial condition.

Here, we present snapshots of the population structure and velocity fields obtained in DES at three stages of colony growth and ordering. Figs. S3 and S4 depict the colony structure and velocity vector fields for the pressure-independent and pressure-dependent cell growth cases, respectively. Simulations were performed for a long channel with aspect ratio, $A = 4.0$, starting from the low packing fraction, $\rho_0 = 0.02$. Snapshots correspond to times $(a)$ $t = 4.3\tau$ min, $(b)$ $t = 5.7\tau$ min, and $(c)$ $t = 16.4\tau$ min. Clearly, pressure-dependent growth results in a higher degree of ordering and a reduction in observed "swirls."

Finally, Fig. S5 shows the growth of a bacterial colony from a localized initial condition rather than a uniformly seeded condition. The expansion of the colony in the open channel again leads to nematic ordering of the population, demonstrating the applicability of our findings to colonies started from single cells.


1. Cookson S, Ostroff N, Pang WL, Volfson D, Hasty J (2005) Monitoring dynamics of single-cell gene expression over multiple cell cycles. *Mol Sys Biol* 1: msb4100032–E1–msb4100032–E6.
2. Tesla N (1920) US Patent 1,329:559.
3. Duffy DC, Schueller OJA, Brittain ST, Whitesides GM (1999) Rapid prototyping of microfluidic switches in poly(dimethyl siloxane) and their actuation by electro-osmotic flow. *J Micromech Microeng* 9:211–217.
4. Bendib S, Francais O (2001) Analytical study of microchannel and passive microvalve application to micropump simulator. *Proc. SPIE* 4593:283–291.

5. Gui L, Merzkirch W (1996) A method of tracking ensembles of particle images. *Exp Fluids* 21:465–468.
6. Cowen EA, Sveen JK (2003) Quantitative imaging techniques and their application to wavy flows. *PIV and Water Waves*, eds Grue J, Liu PLF, Pedersen G (World Scientific, Teaneck, NJ), pp 1–49.
7. Doi M, Edwards SE (2003) *The Theory of Polymer Dynamics* (Oxford Univ Press, Oxford).
8. de Gennes P, Prost J (1993) *The Physics of Liquid Crystallgraphy* (Clarendon, Oxford), 2nd Ed.
9. Olmsted PD, Goldbart P (1992) Isotropic-nematic transition in shear flow: State selection, coexistence, phase transitions, and critical behavior. *Phys Rev A* 46:4966–4993.
10. Shraiman BI (2005) Mechanical feedback as a possible regulator of tissue growth. *Proc Natl Acad Sci USA* 102:3318–3323.
11. Volfson D, Tsimring LS, Kudrolli A (2004) Anisotropy driven dynamics in vibrated granular rods. *Phys Rev E* 70:051312.
12. Rapaport DC (2004) *The Art of Molecular Dynamics Simulation* (Cambridge Univ Press, Cambridge, UK).
13. Schäfer J, Dippel S, Wolf DE (1996) Force schemes in simulations of granular materials. *J Phys I France* 6:5–20.

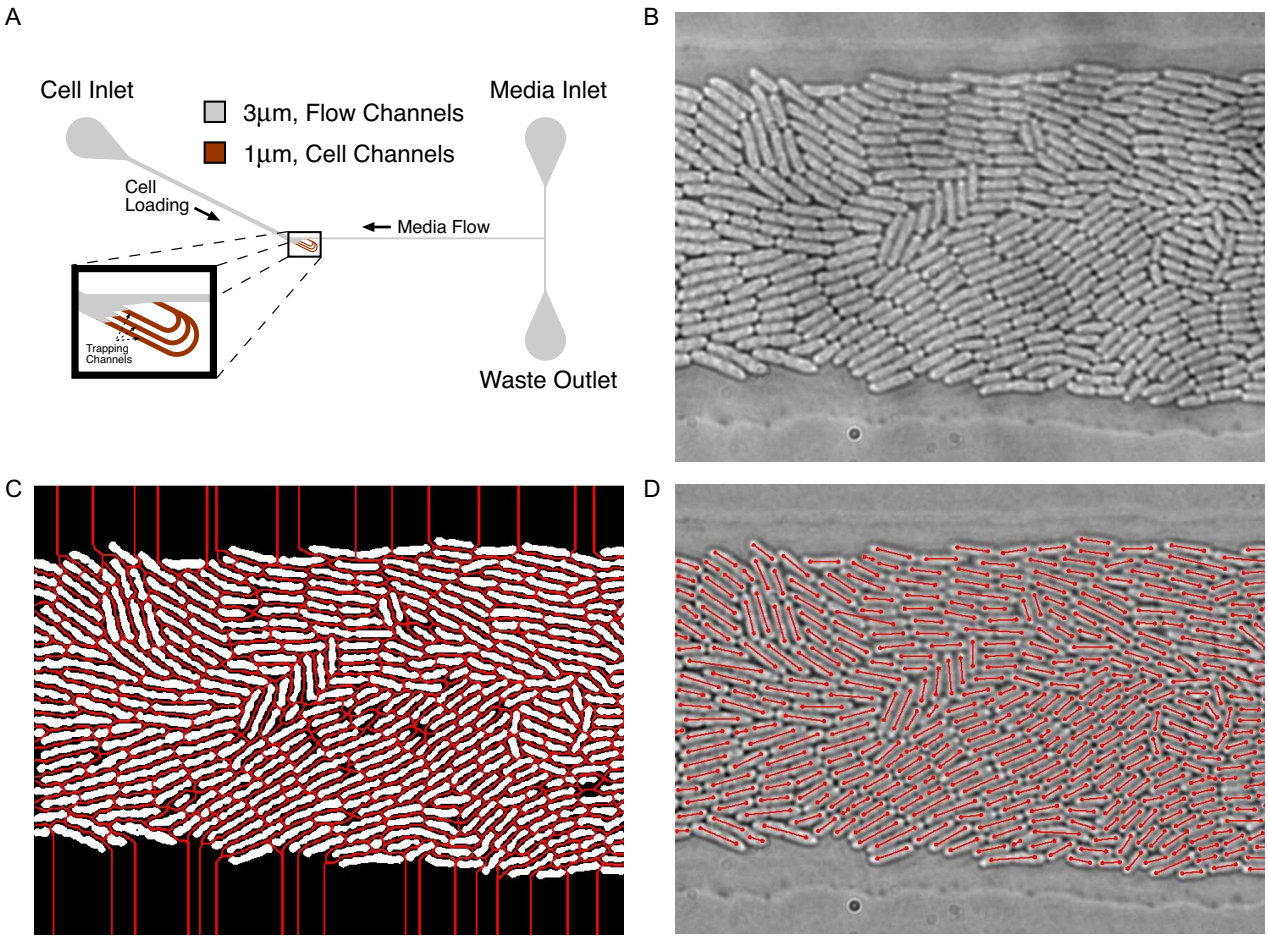


**Fig. S1.** Microfluidic device design and image processing. (*A*) Schematic diagram of the microfluidic device adapted to study *E. coli* ordering in open channels. (*B–D*) Image processing steps: original bright-field image (*B*), construction of a binary mask and watershedding (*C*), and recognition (*D*). The lengths of red segments are proportional to the sizes of cells.

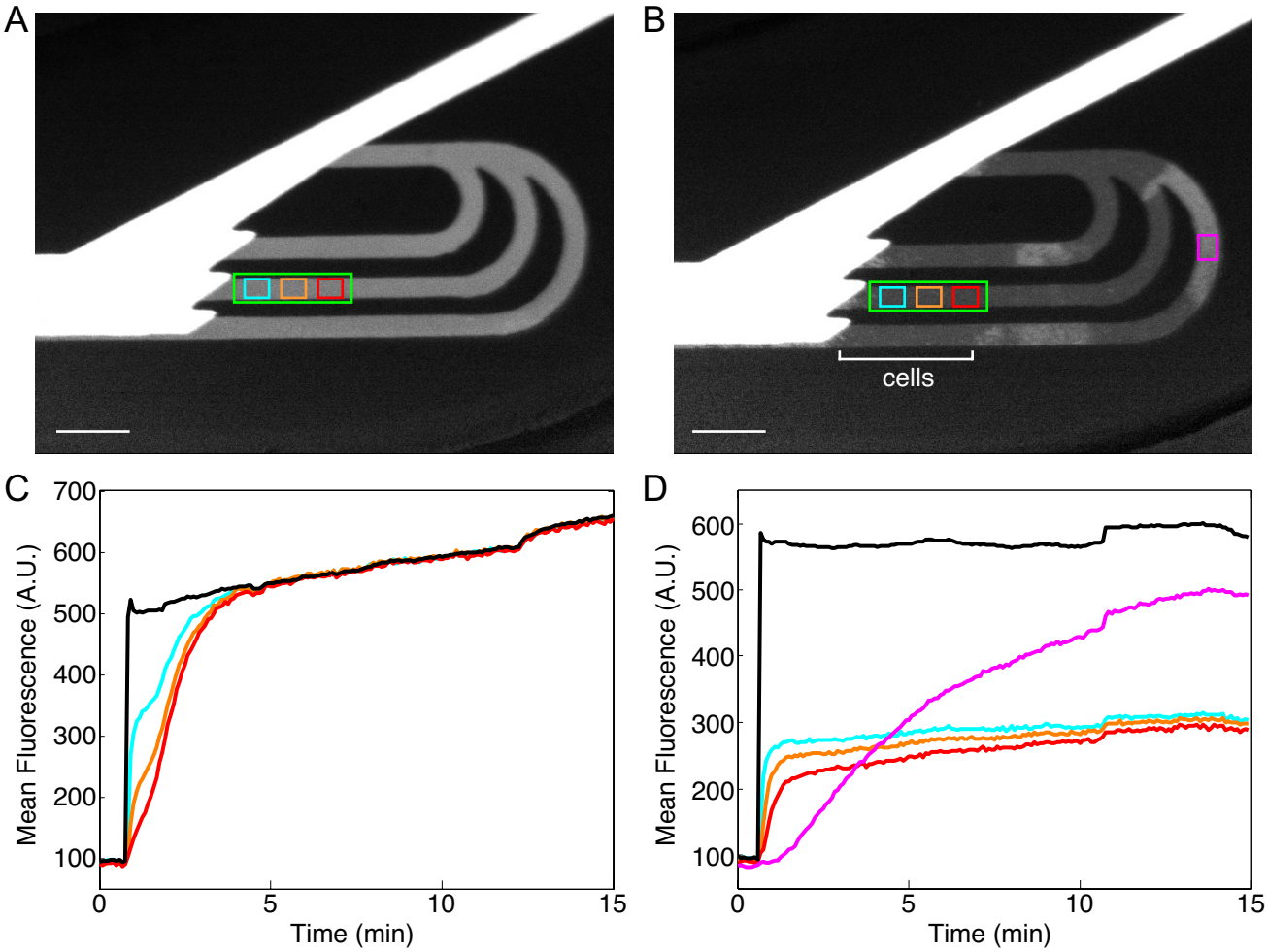


**Fig. S2.** Experimental results for the diffusion of fluorescent dye within the chamber. (*A* and *B*) Snapshots of fluorescence after dye propagation throughout the cell-free system (*A*) and the cell-packed system (*B*). Fluorescence is brighter in the deep (3 $\mu$m) bypass channel but still nearly uniform in the shallow (1 $\mu$m) cell trapping area. (*C* and *D*) Time series plots of fluorescence averaged over identical areas in the bypass channel (black) and in three regions of the experimental field of view (cyan, orange, and red boxes) after dye introduction. Intensity in the bypass channel has been rescaled by a factor of 1:2.5 to match the intensity of dye in the empty cell trapping area. Additionally, a time series of the averaged intensity in an empty pocket of the cell-trapping region is shown in *d* in magenta. (Scale bars: 100 $\mu$m.)

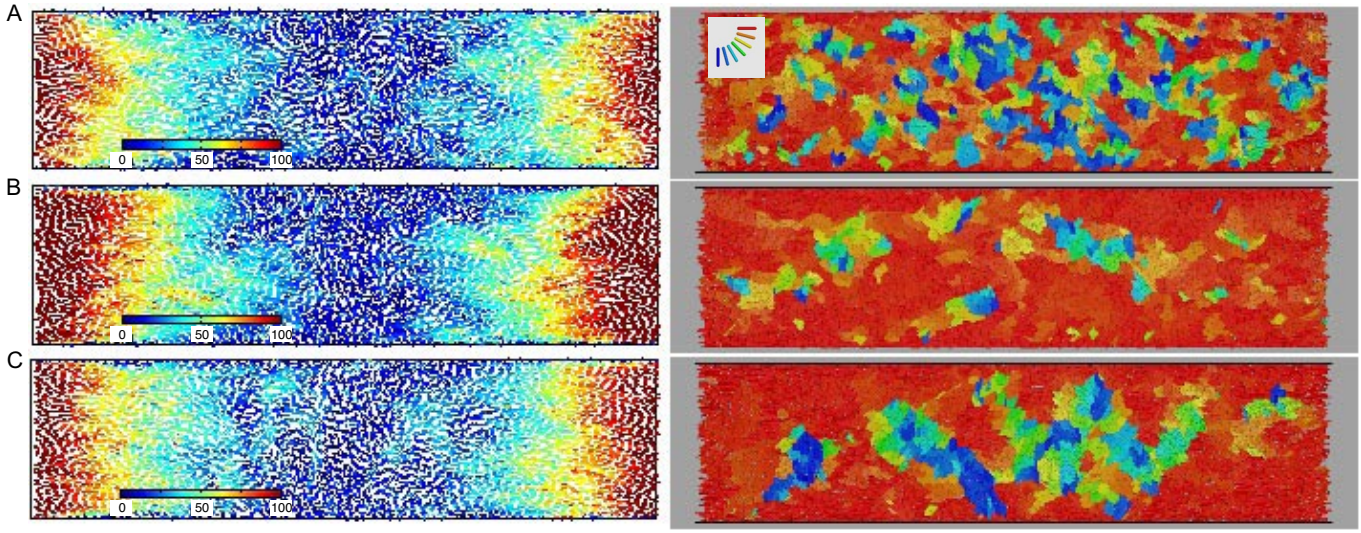


**Fig. S3.** DES of bacterial growth in a colony with a pressure-independent growth rate (model C1) and a channel aspect ratio of $A = 4.0$. (*Left*) Snapshots of the colony structure in the system show velocity vector fields. Each vector corresponds to the instantaneous translational velocity of a cell, where length is normalized for visual clarity and colors (from blue to red) correspond to magnitude (from low to high). (*Right*) Cell orientation maps. Cell color denotes orientation relative to the channel axis, from blue (perpendicular) to red (parallel). (*A*) $t = 4.3\tau$ min. (*B*) $t = 5.7\tau$ min. (*C*) $t = 16.4\tau$ min. $\tau = 20$ min is the division time.

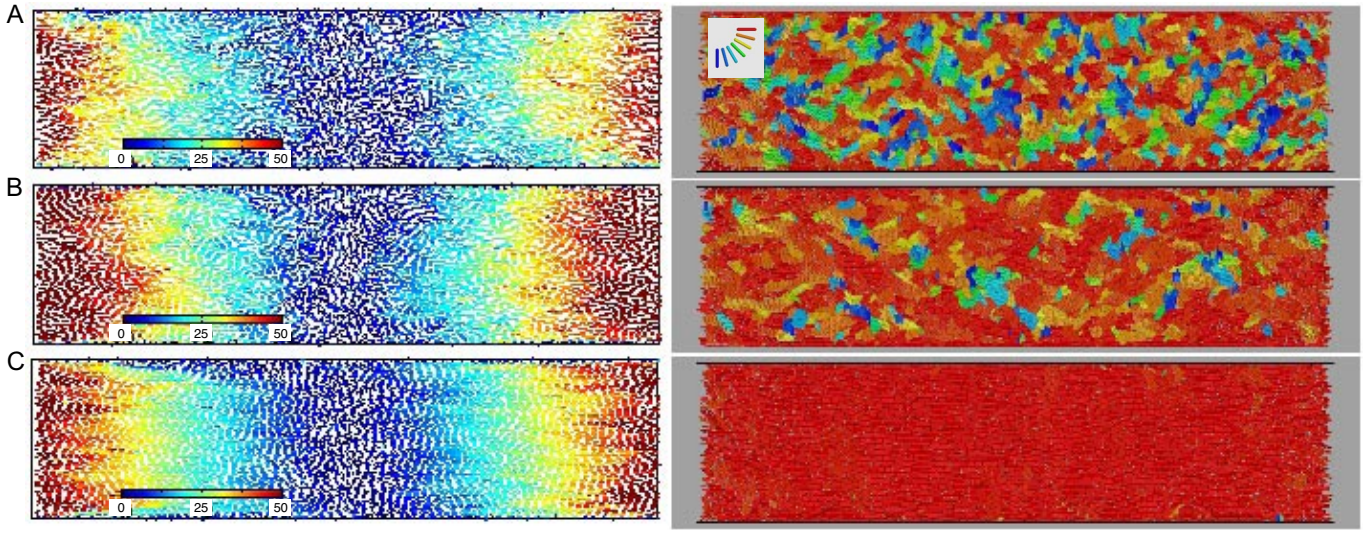


**Fig. S4.** DES of bacterial growth in a colony with a pressure-dependent growth rate (model C2) and a channel aspect ratio of $A = 4.0$. Snapshots of colony structure are synchronous to the system shown in Fig. S3, but with $\alpha_0 = 0.7128$ and $p_c = \sigma_{xx} + \sigma_{zz} = 2 \cdot 10^5$.

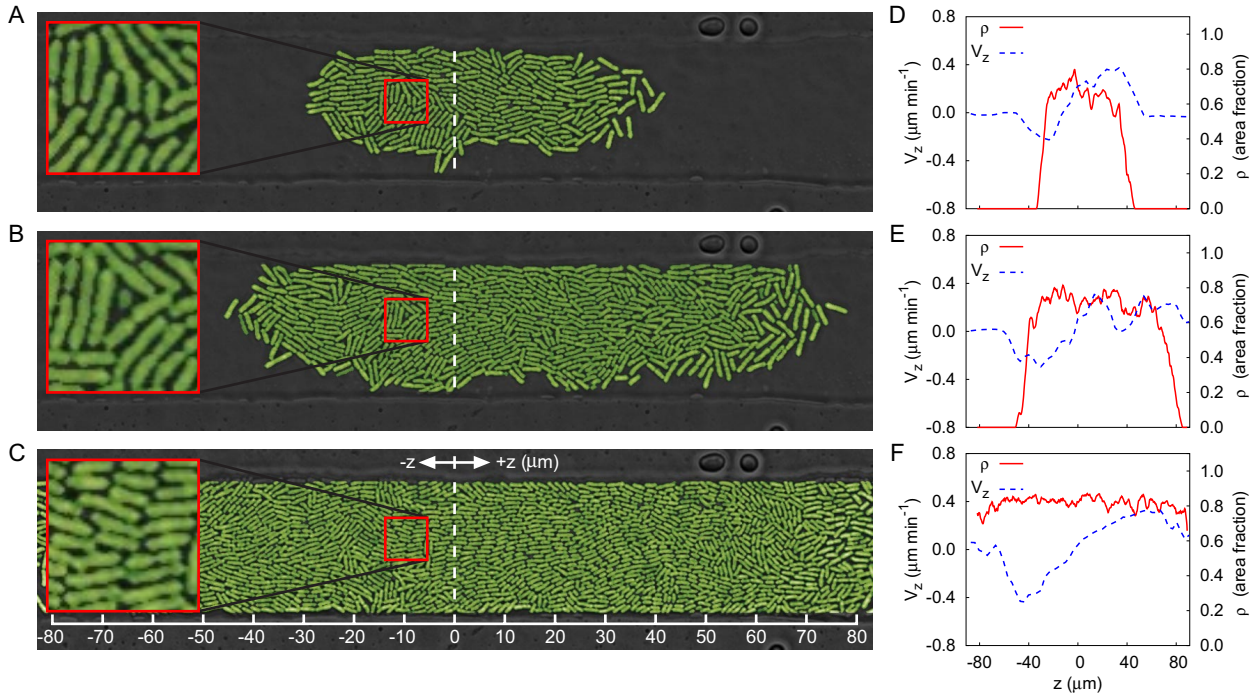


**Fig. S5.** Experimental results for bacterial growth and ordering from a single initial cell. (*A–C*) Three snapshots of *E. coli* monolayer growth and ordering in a quasi-2D open microfluidic cavity taken at 169, 198, and 248 min from the beginning of the experiment. (*D–F*) Velocity and density profiles along the channel corresponding to the snapshots in *A–C*.